

A fast boundary integral method for high-order multiscale mesh generation

Felipe Vico¹

*Instituto de Telecomunicaciones y Aplicaciones Multimedia (ITEAM)
Universidad Politècnica de València
València, Spain 46022
felipe.vico@gmail.com*

Leslie Greengard²

*Courant Institute
New York University
New York, NY, 10012
greengard@cims.nyu.edu*

*Center for Computational Mathematics
Flatiron Institute
New York, NY 10010*

Michael O'Neil^{3,4}

*Courant Institute
New York University
New York, NY 10012
oneil@cims.nyu.edu*

Manas Rachh

*Center for Computational Mathematics
Flatiron Institute
New York, NY 10010
mrachh@flatironinstitute.org*

¹Research supported in part by the Office of Naval Research under award numbers #N00014-18-1-2307.

²Research supported in part by the Office of Naval Research under award numbers #N00014-18-1-2307.

³Research supported in part by the Office of Naval Research under award numbers #N00014-17-1-2059, #N00014-17-1-2451, and #N00014-18-1-2307.

⁴Corresponding author.

Abstract

In this work we present an algorithm to construct an infinitely differentiable smooth surface from an input consisting of a (rectilinear) triangulation of a surface of arbitrary shape. The original surface can have non-trivial genus and multiscale features, and our algorithm has computational complexity which is linear in the number of input triangles. We use a smoothing kernel to define a function Φ whose level set defines the surface of interest. Charts are subsequently generated as maps from the original user-specified triangles to \mathbb{R}^3 . The degree of smoothness is controlled locally by the kernel to be commensurate with the fineness of the input triangulation. The expression for Φ can be transformed into a boundary integral, whose evaluation can be accelerated using a fast multipole method. We demonstrate the effectiveness and cost of the algorithm with polyhedral and quadratic skeleton surfaces obtained from CAD and meshing software.

Keywords: High-order surface discretization, level set, fast multipole method, mesh generation, boundary integrals.

Contents

1	Introduction	2
2	Smooth surfaces via multiscale mollification	4
3	Constructing an atlas	6
3.1	Local coordinates	8
3.2	High-order approximation	9
4	Computing the level set function	10
4.1	Surface integral representation	11
4.2	Numerical evaluation of σ	12
4.3	Numerical evaluation of Φ	12
4.4	Fast multipole acceleration	13
4.5	Surface refinement	14
5	Numerical examples	14
5.1	Basic surface construction	16
5.2	Recovery of a sphere	16
5.3	Quadratic skeletons	19
5.4	Large-scale structures	19
5.5	Modes of failure	19
6	Conclusions	23

1 Introduction

Over the past two decades, high-order accurate methods have been developed for solving many of the partial differential equations (PDEs) of classical mathematical physics in complicated geometries. These include the equations that govern electromagnetics, electrostatics, acoustics, fluid dynamics, and heat flow. In two dimensions, the state of the art is quite advanced, in the sense that the combination of high-order representations of the domain, high-order discretization methods, and fast algorithms have permitted near machine precision accuracy using a modest number of unknowns. For constant-coefficient, homogeneous equations, which can easily be reformulated as boundary integral equations, it is sufficient to have a high-order representation of the boundary itself. After discretization of the weakly-singular or singular integral operators using high-order quadratures, see [31] and the review [22], the resulting linear systems can be solved in optimal, or nearly optimal, time using fast multipole methods (FMMs) or related fast algorithms (see, for example, [19, 20, 23, 28]).

The state of the art is quite different in the three-dimensional setting. Standard boundary integral or boundary element methods often use piecewise constant or linear approximations of boundary densities defined on flat triangulated surfaces to discretize integral operators. Since fast algorithms [4, 7, 9, 12, 21, 30, 37, 42] and high-order accurate quadrature schemes [5, 6, 35, 40] are available, it is the lack of suitable surface representations that has hampered the development of accurate fast solvers in general geometries. In practice, the high-order geometries that can be accessed are those for which an analytic parametrization is available (such as a deformed sphere or torus) [5, 29], or ones for which considerable effort has been expended in defining a smooth surface. Existing meshing algorithms which *do* generate high-order curvilinear triangles or quadrilateral patches, such as Gmsh [18], require a computer aided design-compatible geometry as input.

In the present paper, we describe an algorithm to construct an infinitely differentiable smooth surface from an input consisting of a (rectilinear) triangulation of a surface of arbitrary shape. The original surface can have non-trivial genus and multiscale features, and the running time of our algorithm is linear in the number of input triangles. We use a target-dependent (non-translation invariant) smoothing kernel whose integral over the interior of the domain of interest defines a function Φ whose level set $\Phi = 1/2$ will be used as the definition of its C^∞ surface approximation. Charts are then generated as maps from the original user-specified triangles to \mathbb{R}^3 . The method is able to handle highly non-uniform discretizations by ensuring that the extent of smoothing is commensurate with the local fineness of the triangulation. By application of the divergence theorem, the volume integral defining Φ can be converted into an integral over the triangulated boundary itself; the resulting boundary integral can then be evaluated using the fast multipole method. At the risk of stating the obvious, the impetus behind our work is to reduce the overall cost of solving the PDEs of mathematical physics. High-order accuracy is critical, for example, in large-scale wave propagation problems, but the ability to achieve high-order accuracy is equally critical to enable automatic adaptivity and robust error analysis even for non-oscillatory problems.

There is an extensive literature on mesh generation, mesh repair, surface parameterization, etc. Much of this has been driven by the needs of computer graphics or visualization and we do not seek to review the literature, but we do highlight earlier work that is closest

in spirit to the method presented below. The problem of interest here involves taking as input a water-tight flat triangulation, and creating an infinitely smooth surface (and corresponding high-order triangulation) which is a high-fidelity approximant of the low-order flat triangulation. This problem clearly does not have a unique solution, and we seek simply to create *some* fixed surface which can serve as the underlying smooth surface to which a high-order accurate discretization is converging.

Relevant earlier work includes [11], in which the authors propose a local method for mesh repair (adjusting the size/aspect ratio of mesh elements), based on local interpolation and adjustment of control points. This algorithm is able to generate very high-quality meshes, but is limited to curvilinear second-order triangles. Higher order methods also exist that begin with flat triangulations, or even point clouds in \mathbb{R}^3 . One such scheme is “moving least squares” surface reconstruction (see, for example, [15]). This method proceeds, as the name suggests, by computing a smooth surface based on a local least-squares approximation of the data. It has the advantage of being able to handle point clouds and noisy triangulations, including those obtained from three dimensional scanning devices. We should note that the algorithm below, in its current form, is less general in that it does not handle noise. (We will return to this point in the concluding section.)

Perhaps most closely related to our scheme is a method introduced in the 1990’s, namely that of *convolution surfaces* [3, 33, 34]. Convolution surfaces were inspired by even earlier methods of surface construction used in molecular modeling and animation, based on computing iso-potential surfaces from point sources [2]. The fundamental idea is to generate an implicit surface by computing the convolution of a single radially symmetric Gaussian with the characteristic function of the *surface*. In our scheme, we define a level set function as the convolution of a Gaussian with the characteristic function of the *volume*, with a variance carefully chosen in a target-specific fashion in order to be commensurate with the fineness of the nearby triangles. This enables a multi-scale form of smoothing. Another important class of methods is based on subdivision surfaces [13, 44], which successively refine the triangulation as more and more smoothness is requested. A scheme presented in [43] constructs an atlas based on large parameterized patches, taking as input a polyhedral surface and using partitions of unity to blend them together. Recently, a fast and robust tetrahedral meshing scheme was developed [24], which can also generate smooth surfaces, but its principal goal is the volume mesh, a topic we don’t consider here.

Finally, we should note that important work has been done in the area of isogeometric analysis (IGA) [10, 25, 36] with regard to boundary element and boundary integral equation methods. IGA is a framework for dealing directly with CAD geometries, and provides a robust set of tools for surface refinement, manipulation, and discretization. There have been several PDE and integral equation solvers constructed based on IGA, and significant progress has been made toward coupling computer-aided design (CAD) systems with finite element methods. These schemes are complementary to the method presented below, which assumes no external information about the “true” underlying surface and takes as input only a flat triangulated mesh.

Remark 1. *A precursor of the algorithm presented here is the edge/corner rounding scheme of Epstein and O’Neil [14]. The basic observation in that work is the following: if corners of a polygon $P \subset \mathbb{R}^2$ are viewed locally as maps over the tangent line, then local convolution with a finite width “bell” function results in a smooth curve which preserves convexity and leaves large flat regions unchanged. If the finite-width bell is replaced with a Gaussian which*

has decayed to magnitude ϵ , then the resulting geometry is an ϵ -accurate approximation to a true C^∞ curve. While this scheme could be extended to an arbitrary three-dimensional geometry (the extension is, in fact, also described in [14]), it would require the separate calculation of many local maps which would have to be patched together. By reformulating the problem in terms of a volume integral with a C^∞ kernel, no local maps need to be constructed, while retaining the useful features of the edge/corner rounding formalism.

The paper is organized as follows: in Section 2, we construct a multiscale mollifier for defining the smooth surface. In Section 3, we introduce the mathematical foundations for defining an implicit surface as a level set and for constructing the corresponding atlas. In Section 4, we describe a fast algorithm for constructing the level set and its charts. Section 5 contains some numerical examples demonstrating the efficiency and behavior of the algorithm, and we conclude with a discussion of future work in Section 6.

2 Smooth surfaces via multiscale mollification

Let $V \subset \mathbb{R}^3$ be a closed and bounded region with orientable boundary S , and let $K : \mathbb{R}^3 \rightarrow \mathbb{R}$ be a C^∞ mollifier - that is, a compactly supported function with

$$\begin{aligned} \int_{\mathbb{R}^3} K(\mathbf{x}) d\mathbf{x} &= 1, \\ \lim_{\epsilon \rightarrow 0} \frac{K(\mathbf{x}/\epsilon)}{\epsilon^3} &= \delta(\mathbf{x}), \end{aligned} \tag{2.1}$$

where $\delta(\mathbf{x})$ is the Dirac delta function. For simplicity we will define K_ϵ to be this scaled version of K :

$$K_\epsilon(\mathbf{x}) = \frac{K(\mathbf{x}/\epsilon)}{\epsilon^3}. \tag{2.2}$$

It is well-known [17] that

$$\begin{aligned} \Phi(\mathbf{x}) &= \int_{\mathbb{R}^3} K_\epsilon(\mathbf{x} - \mathbf{x}') \mathbf{1}_V(\mathbf{x}') d\mathbf{x}' \\ &= \int_V K_\epsilon(\mathbf{x} - \mathbf{x}') d\mathbf{x}' \end{aligned} \tag{2.3}$$

is itself a C^∞ function, defined in all of \mathbb{R}^3 , where $\mathbf{1}_V$ is the characteristic function of V . The level sets $\Phi = C$ define smooth surfaces embedded in \mathbb{R}^3 , and will be denoted by Γ_C . The region bounded by Γ_C will be denoted as Ω_C . Moreover, interior regions of flat subsets of S which are larger than the support of the kernel K_ϵ are preserved along $\Gamma_{1/2}$. This is easy to show in the one-dimensional case [14], and straightforward to prove in higher dimensions. If V is convex, then $\Gamma_{1/2}$ defines a *numerically-convex* region, in which the deviation from convexity is on the scale of the square-root of the second moment of the kernel (akin to the standard deviation). Because of these properties, in the remainder of this paper, we will define the smooth surface via the level set $\Gamma_{1/2}$.

Rather than using a mollifier in the strict mathematical sense (i.e. one that is compactly supported), it is very convenient for numerical purposes to replace K_ϵ with the Gaussian kernel G_σ :

$$G_\sigma(\mathbf{x}) = \frac{e^{-\|\mathbf{x}\|^2/2\sigma^2}}{(2\pi\sigma^2)^{3/2}}, \tag{2.4}$$

and redefine Φ using this kernel so that

$$\Phi(\mathbf{x}) = \int_{\mathbb{R}^3} G_\sigma(\mathbf{x} - \mathbf{x}') \mathbf{1}_V(\mathbf{x}') d\mathbf{x}' = \int_V G_\sigma(\mathbf{x} - \mathbf{x}') d\mathbf{x}'. \quad (2.5)$$

Above, Φ can be physically interpreted via heat flow: $\Phi(\mathbf{x})$ is the temperature at $\mathbf{x} \in \mathbb{R}^3$ at time $\sigma^2/2$, assuming that the temperature at time zero is given by 1 for $\mathbf{x} \in V$ and zero otherwise. Therefore, larger values of σ (i.e. time) result in smoother distributions of temperature.

The problem with this approach to surface generation as a general-purpose tool, however, is that the single parameter ϵ or σ determines a uniform length scale of smoothing. In geometries with multiscale features (involving triangles of vastly different sizes), no single choice of ϵ or σ can be effective qualitatively or numerically: the method would either fail to adequately smooth regions with large triangles, or it would wash out features in regions with small triangles. Thus, instead of (2.5), we will define Φ by

$$\Phi(\mathbf{x}) = \int_V G(\mathbf{x} - \mathbf{x}', \sigma(\mathbf{x})) d\mathbf{x}', \quad (2.6)$$

where

$$G(\mathbf{x} - \mathbf{x}', \sigma(\mathbf{x})) = \frac{e^{-\|\mathbf{x} - \mathbf{x}'\|^2/2\sigma(\mathbf{x})^2}}{(2\pi\sigma(\mathbf{x})^2)^{3/2}}, \quad (2.7)$$

and $\sigma(\mathbf{x})$ is chosen to be commensurate with the size of the triangle on S which is closest to \mathbf{x} . We now turn to the actual construction of the non-constant σ above.

The multiscale mollifier

In order for the surface $\Gamma_{1/2}$ to be C^∞ , the variance of the kernel G , i.e. the function $\sigma = \sigma(\mathbf{x})$ in (2.7), must be C^∞ . Furthermore, σ should be non-oscillatory in order to preserve the convexity of the domain as much as possible. While there are many possibilities of constructing such a function, we use the following formulation, which works well in practice for surfaces with multiscale features.

Suppose that S , which we will also refer to as the *skeleton surface*, is given as the union of M triangles T^j , $j = 1, 2, \dots, M$. Let \mathbf{c}_j denote the centroid of T^j and let $\sigma_j = D_j/\lambda$, where D_j is the diameter of T^j (i.e. the diameter of the smallest ball which encloses T^j), and λ is a free parameter. We then define σ as:

$$\sigma(\mathbf{x}) = \frac{\sum_{j=1}^M \sigma_j e^{-\|\mathbf{x} - \mathbf{c}_j\|^2/2\sigma_0^2}}{\sum_{j=1}^M e^{-\|\mathbf{x} - \mathbf{c}_j\|^2/2\sigma_0^2}}, \quad (2.8)$$

where σ_0 is a second free parameter. Note that the dominant term in the sum in the numerator is due to the nearest centroid \mathbf{c}_j to the point \mathbf{x} ; other contributions decay exponentially fast. It is useful to set these parameters such that the influence on a triangle T due to triangles T^j of the same size, but outside T 's immediate nearest neighbors, is nearly negligible. Ultimately, λ controls the smoothness of the final surface and σ_0 controls the smoothness of σ itself. In practice, reasonable choices for the free parameters above are

$$\lambda \approx 2.5, \quad \sigma_0 \approx \sqrt{5} \max_j D_j. \quad (2.9)$$

Using these values, the influence on σ of triangles separated by a diameter is roughly 0.5 (due to the choice of σ_0), and σ has decayed to approximately 10^{-9} at a distance of 2.5 diameters from the centroid (as determined by λ). Such a choice enables a straightforward splitting of the near field and far field of triangle T when embedded in an octree data structure (see Section 4.4). With the above observations in mind, and the formula for computing Φ in (2.6), we now turn to the construction of an atlas defining the C^∞ as a collection of charts from the input skeleton triangulation.

3 Constructing an atlas

In this section, we present a method for constructing an atlas (i.e. a collection of charts or parameterizations) for $\Gamma_{1/2}$. Recall that the skeleton surface S is given as the union of M triangles T^j , $j = 1, \dots, M$. For each triangle T^j , we denote its three vertices by $\{\mathbf{P}_1^j, \mathbf{P}_2^j, \mathbf{P}_3^j\}$. We assume this triangulation of S is water-tight, positively oriented, and conforming (by conforming, we mean here that triangles which touch either share a common edge or meet only at a triangle vertex. It is straightforward to extend our construction to other configurations, including quadrilateral patches, non-conforming triangulations, etc.).

Each skeleton triangle can be parameterized as:

$$\mathbf{T}^j(u, v) = \mathbf{P}_1^j + u(\mathbf{P}_2^j - \mathbf{P}_1^j) + v(\mathbf{P}_3^j - \mathbf{P}_1^j), \quad (3.1)$$

with a local basis for \mathbb{R}^3 defined by

$$\mathbf{T}_u^j = \mathbf{P}_2^j - \mathbf{P}_1^j, \quad \mathbf{T}_v^j = \mathbf{P}_3^j - \mathbf{P}_1^j, \quad \mathbf{N}^j = \mathbf{T}_u^j \times \mathbf{T}_v^j. \quad (3.2)$$

In (3.1), (u, v) must lie in the standard simplex triangle

$$T_0 = \{(u, v) \mid u \geq 0, v \geq 0, (u + v) \leq 1\}. \quad (3.3)$$

Note that above, surfaces in \mathbb{R}^3 , such as T^j , are denoted using standard weight font, and vectors, such as \mathbf{T}^j , are denoted in boldface. The normalized versions of the above vectors will be given as $\hat{\mathbf{T}}_u^j, \hat{\mathbf{T}}_v^j, \hat{\mathbf{N}}^j$ (in general, the vectors $\hat{\mathbf{T}}_u^j$ and $\hat{\mathbf{T}}_v^j$ are not orthogonal).

We now wish to construct a *mapping direction* \mathbf{H}^j along triangle T^j such that the level surface $\Gamma_{1/2}$ can be parametrized as the union of curved triangular patches Γ^j , and therefore $\Gamma_{1/2} = \cup_{j=1}^M \Gamma^j$, through the charts

$$\mathbf{x}^j(u, v) = \mathbf{T}^j(u, v) + h^j(u, v) \mathbf{H}^j(u, v), \quad (3.4)$$

where $\mathbf{x}^j : T_0 \rightarrow \Gamma^j$, and $h_j(u, v)$ is determined so that $\mathbf{x}^j \subset \Gamma_{1/2}$. For this to be possible, the mapping direction must not only be continuous along S , but imply a bijective mapping from S to $\Gamma_{1/2}$. Thus, we cannot use the triangle normals \mathbf{N}^j themselves, since they are discontinuous across triangle edges and would yield gaps in the atlas defining the smooth surface. However, a continuous mapping direction, which we refer to as the *pseudonormal* vector field can be constructed on each triangle as follows.

Definition 1. Let \mathbf{P} be a vertex on the skeleton surface S . The set of triangles for which \mathbf{P} is a common vertex is denoted by $\mathcal{T}(\mathbf{P})$. The vertex angle $\theta_{\mathbf{P}}(T)$ of triangle $T \in \mathcal{T}(\mathbf{P})$ is defined to be the interior angle of T at this vertex.

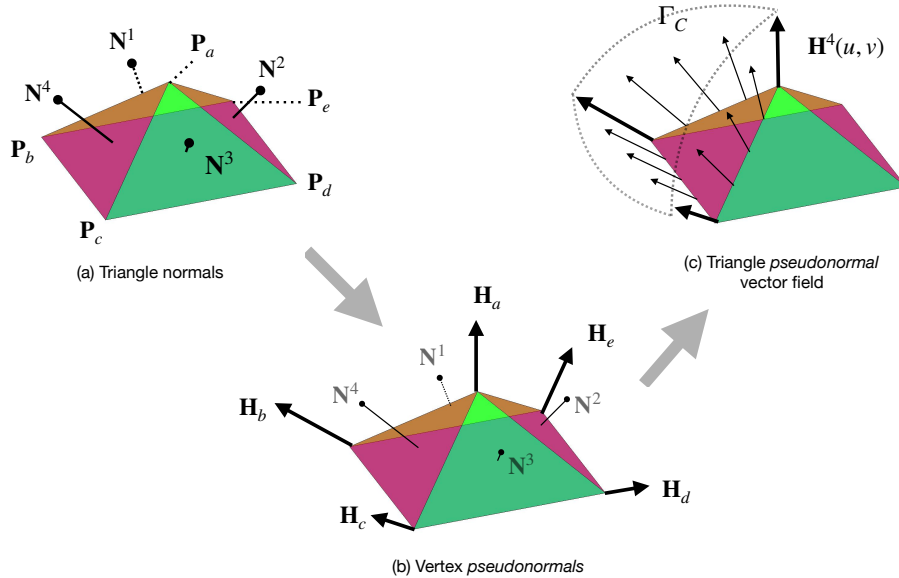


Figure 1: In (a), we show vertex P_a and the other vertices $P_b, P_c, P_d,$ and P_e of the four triangles impinging on it. The normal vectors to the four triangles are denoted by N_1, \dots, N_4 . In (b), we show the vertex pseudonormals, constructed according to (3.6). In (c), we plot the pseudonormal vector field $H^4(u, v)$ along the edges of triangle 4, constructed according to (3.7). We also show a portion of the level set $\Gamma_{1/2}$, which will be represented using (3.4). (Note: The triangles depicted here are not a good approximation of an underlying smooth surface, and serve only as an illustration.)

Definition 2. Let \mathbf{P} be a vertex on the skeleton surface S , and let $A(\mathbf{P})$ denote the total vertex angle at \mathbf{P} :

$$A(\mathbf{P}) = \sum_{T \in \mathcal{T}(\mathbf{P})} \theta_{\mathbf{P}}(T). \quad (3.5)$$

The vertex pseudonormal $\mathbf{H}(\mathbf{P})$ is then given by

$$\mathbf{H}(\mathbf{P}) = \frac{1}{A(\mathbf{P})} \sum_{T \in \mathcal{T}(\mathbf{P})} \theta_{\mathbf{P}}(T) \hat{\mathbf{N}}(T), \quad (3.6)$$

where $\hat{\mathbf{N}}(T)$ is the unit normal along triangle T . Furthermore, on triangle T^j , let the vertex pseudonormals corresponding to its vertices $\{\mathbf{P}_1^j, \mathbf{P}_2^j, \mathbf{P}_3^j\}$ be denoted by $\{\mathbf{H}_1^j, \mathbf{H}_2^j, \mathbf{H}_3^j\}$. Then, the pseudonormal vector field for triangle T^j is defined by the convex combination:

$$\mathbf{H}^j(u, v) = \mathbf{H}_1^j + u(\mathbf{H}_2^j - \mathbf{H}_1^j) + v(\mathbf{H}_3^j - \mathbf{H}_1^j), \quad (3.7)$$

where (u, v) lies on the standard simplex triangle. See Figure 1 for a depiction. We will refer to the function h^j in (3.4) as the pseudonormal distance function.

In short, the vertex pseudonormal is a weighted average of the normals of all triangles impinging on that particular vertex, and the pseudonormal vector field is continuous on S . We note that there are many possible definitions for the weighted average used to define the vertex pseudonormals. For any such choice, the construction in (3.7) yields a continuous vector field on S .

Turning now to the pseudonormal distance function h^j , it is clearly determined point-wise on triangle T^j as the function h^j which satisfies the scalar equation

$$\Phi\left(\mathbf{T}^j(u, v) + h^j(u, v) \mathbf{H}^j(u, v)\right) - \frac{1}{2} = 0. \quad (3.8)$$

The solution to (3.8) can easily be found using Newton's method, for which we will require the evaluation of the directional derivative of Φ :

$$\frac{\partial \Phi}{\partial h^j}(u, v) = \mathbf{H}^j(u, v) \cdot \nabla \Phi(\mathbf{T}^j(u, v) + h^j(u, v) \mathbf{H}^j(u, v)). \quad (3.9)$$

An expression for $\nabla \Phi$ can be determined directly from its integral representation in (2.6). Once h^j is known, the final surface is obtained as the collection of the corresponding charts \mathbf{x}^j , $j = 1, 2, \dots, M$. The previous discussion implies that the function h^j has been computed for every possible u, v , or that it is computed when needed for each u, v . Shortly, in Section 3.2, we detail exactly where and how h^j is evaluated.

3.1 Local coordinates

Our motivating discussion in the introduction laid out the requirements for high-order boundary integral equation solvers in three dimensions. If the surface constructed via the method of this paper is to be used as a high-order geometry processing algorithm, we will also require suitable expressions for the area element and surface tangents on each patch Γ^j of the level surface $\Gamma_{1/2}$. Recall that the chart for the patch Γ^j is given by

$$\mathbf{x}^j(u, v) = \mathbf{T}^j(u, v) + h^j(u, v) \mathbf{H}^j(u, v). \quad (3.10)$$

Taking the partial derivative with respect to u above, we have

$$\begin{aligned} \mathbf{x}_u^j(u, v) &= \frac{\partial \mathbf{x}^j}{\partial u}(u, v) \\ &= \mathbf{T}_u^j(u, v) + h^j(u, v) \mathbf{H}_u^j(u, v) + \frac{\partial h^j}{\partial u}(u, v) \mathbf{H}^j(u, v). \end{aligned} \quad (3.11)$$

Here, $\partial h^j / \partial u$ is unknown, since it was only h^j that was determined via Newton's method. However, using the fact that \mathbf{x}_u^j is tangent to the surface $\Gamma_{1/2}$, and that $\nabla \Phi$ is normal to Γ (by the definition of a level set), we have

$$\frac{\partial h^j}{\partial u} = -\frac{(\mathbf{T}_u^j + h^j \mathbf{H}_u^j) \cdot \nabla \Phi}{\mathbf{H}^j \cdot \nabla \Phi}. \quad (3.12)$$

A similar calculation can be used to obtain

$$\mathbf{x}_v^j = \mathbf{T}_v^j + h^j \mathbf{H}_v^j + \frac{\partial h^j}{\partial v} \mathbf{H}^j \quad (3.13)$$

where

$$\frac{\partial h^j}{\partial v} = -\frac{(\mathbf{T}_v^j + h^j \mathbf{H}_v^j) \cdot \nabla \Phi}{\mathbf{H}^j \cdot \nabla \Phi}. \quad (3.14)$$

The area element on Γ^j is easily computed from the definition

$$da = |\mathbf{x}_u^j \times \mathbf{x}_v^j| du dv, \quad (3.15)$$

and the normal vector, as noted above, is given by $\nabla\Phi$.

Depending on the application [29], it may be necessary to compute higher order derivatives of the surface parameterization. These derivatives can be obtained via a computation similar to that used in obtaining first derivatives. Consider the calculation of the second order partial derivative $\mathbf{x}_{uu}^j(u, v)$. Taking the derivative of both sides of (3.11) with respect to u we have:

$$\mathbf{x}_{uu}^j(u, v) = \mathbf{T}_{uu}^j(u, v) + h^j(u, v) \mathbf{H}_{uu}^j(u, v) + 2h_u^j(u, v) + h_{uu}^j(u, v) \mathbf{H}_u^j(u, v). \quad (3.16)$$

In the expression above the only unknown term is $h_{uu}^j(u, v)$. This term can be obtained by differentiating both sides of equation (3.8) twice:

$$\begin{aligned} & \left(\mathbf{T}_u^j + h_u^j \mathbf{H}^j + h^j \mathbf{H}_u^j \right)^T \nabla \nabla \Phi \left(\mathbf{T}_u^j + h_u^j \mathbf{H}^j + h^j \mathbf{H}_u^j \right) + \\ & \quad + \nabla \Phi \cdot \left(\mathbf{T}_{uu}^j + 2h_u^j \mathbf{H}_u^j + h \mathbf{H}_{uu}^j + h_{uu} \mathbf{H}^j \right) = 0, \end{aligned} \quad (3.17)$$

where $\nabla \nabla \Phi$ is the Hessian matrix of the function Φ . Then, solving for h_{uu}^j we get:

$$\begin{aligned} h_{uu}^j = & - \frac{\left(\mathbf{T}_u^j + h_u^j \mathbf{H}^j + h^j \mathbf{H}_u^j \right)^T \nabla \nabla \Phi \left(\mathbf{T}_u^j + h_u^j \mathbf{H}^j + h^j \mathbf{H}_u^j \right)}{\nabla \Phi \cdot \mathbf{H}^j} \\ & - \frac{\nabla \Phi \cdot \left(\mathbf{T}_{uu}^j + 2h_u^j \mathbf{H}_u^j + h \mathbf{H}_{uu}^j \right)}{\nabla \Phi \cdot \mathbf{H}^j}. \end{aligned} \quad (3.18)$$

Similar expressions for \mathbf{x}_{uv}^j , \mathbf{x}_{vv}^j , or any arbitrary higher order derivative of the surface, can be derived (of course the algebra becomes rather unwieldy rather quickly). Using these higher order derivatives, it becomes possible to obtain the second fundamental form of the surface, Gaussian/mean curvatures, Christoffel symbols, and other quantities of interest in differential geometry. These quantities are often used in time dependent PDEs to determine the evolution of free boundaries. Special care may need to be used when numerically computing these higher derivatives, but schemes are necessarily case-dependent.

3.2 High-order approximation

We now seek to develop a high-order approximation of the surface $\Gamma_{1/2}$ as a collection of piecewise smooth charts. To this end, we will approximate each component of each chart $\mathbf{x}^j : T_0 \rightarrow \Gamma^j$ in (3.4) as a polynomial in $u, v \in T_0$ of total degree p . Each chart will be referred to as a p th-order curvilinear triangle, or p th-order approximant. This can be achieved by a method analogous to polynomial interpolation/approximation in one dimension: the function \mathbf{x}^j will be sampled at the p th-order Vioreanu-Rokhlin nodes on T_0 , which provide stable interpolation formulae for high-order polynomial approximation on the simplex T_0 [39]. Polynomial approximation and interpolation is performed using an orthogonal basis of Koornwinder polynomial [27], analogous to using Legendre polynomials on the interval $[-1, 1]$. Note that in contrast to some computational geometry procedures for determining surfaces, no effort is made to match values or derivatives at interfaces, but rather only to approximate the function to high accuracy on each panel. (And therefore any gaps that may appear in our approximation of $\Gamma_{1/2}$ can be controlled and made to be as small as desired.)

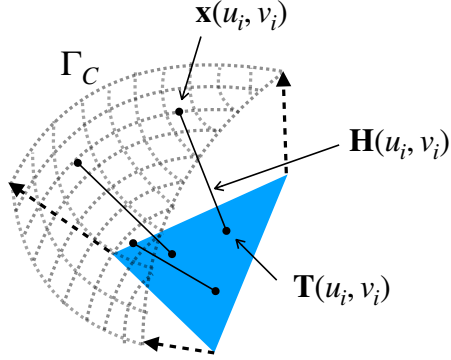


Figure 2: The pseudonormal direction vector $\mathbf{H}(u_i, v_i)$ emanating from the quadrature node $\mathbf{T}(u_i, v_i)$ intersects the level surface Γ_C at $\mathbf{x}(u_i, v_i)$. The distance along $\mathbf{H}(u_i, v_i)$, denoted by h_{ji} is determined using Newton's method.

To this end, we first recall that there are $n_p = (p+1)(p+2)/2$ polynomials of two variables with total degree $\leq p$. Let (u_i, v_i) , $i = 1, 2, \dots, n_p$ denote the p th-order Vioreanu-Rokhlin nodes. As detailed earlier, in order to evaluate $\mathbf{x}^j(u_i, v_i)$ it is necessary to compute the corresponding pseudonormal distance $h^j(u_i, v_i)$ which satisfies:

$$\Phi(\mathbf{x}^j(u_i, v_i)) = \Phi\left(\mathbf{T}^j(u_i, v_i) + h^j(u_i, v_i) \mathbf{H}^j(u_i, v_i)\right) = \frac{1}{2}. \quad (3.19)$$

To simplify the notation, let $h_{ji} = h^j(u_i, v_i)$; then, letting $h_{ji}^{(k)}$ be the k th iterate for computing h_{ji} in Newton's method, we have

$$h_{ji}^{(k+1)} = h_{ji}^{(k)} - \frac{\Phi\left(\mathbf{T}^j(u_i, v_i) + h_{ji}^{(k)} \mathbf{H}^j(u_i, v_i)\right) - 1/2}{\mathbf{H}^j(u_i, v_i) \cdot \nabla \Phi\left(\mathbf{T}^j(u_i, v_i) + h_{ji}^{(k)} \mathbf{H}^j(u_i, v_i)\right)}, \quad (3.20)$$

where we make use of (3.9) for $\partial\Phi/\partial h$. We initialize the Newton iteration with $h_{ji}^{(0)} = 0$. Once Newton's method has converged, the local coordinate system and metric tensor along the surface, with respect to the local parameterizations on T^j , can be calculated using the expressions in Section 3.1.

4 Computing the level set function

Each Newton step for evaluating $h_{ji}^{(k)}$, used in eventually computing the point $\mathbf{x}^j(u_i, v_i) \in \Gamma^j$, requires the evaluation of Φ and its gradient at $n_p M$ target locations (n_p nodes on each of M patches). Thus, in order for the method to be practical, we need to be able to compute the volume integral in (2.6) accurately and rapidly, preferably with a computational cost scaling as $\mathcal{O}(n_p M)$, i.e. the number of interpolation points on $\Gamma_{1/2}$. One option would be to design a variant of the fast Gauss transform (FGT) that combines the hierarchical data structure of [41] with the variable scale FGT of [38]. This, however, would require a surface-conforming volume mesh for the region V and a rather complicated implementation of the fast algorithm. Instead, we will recast (2.6) as a boundary integral and discuss fast algorithms for evaluating the reformulated version of Φ .

4.1 Surface integral representation

The integral representation in (2.6) can be reformulated as a boundary integral along S by a straightforward application of the divergence theorem. First, we observe that

$$\Delta_{\mathbf{x}'} \left(\frac{\operatorname{Erf} \left(\frac{\|\mathbf{x} - \mathbf{x}'\|}{\sqrt{2}\sigma(\mathbf{x})} \right)}{4\pi\|\mathbf{x} - \mathbf{x}'\|} \right) = - \frac{e^{-\|\mathbf{x} - \mathbf{x}'\|^2/2\sigma(\mathbf{x})^2}}{(2\pi\sigma(\mathbf{x}))^{3/2}}, \quad (4.1)$$

where

$$\operatorname{Erf}(r) = \frac{2}{\sqrt{\pi}} \int_0^r e^{-t^2} dt. \quad (4.2)$$

From the preceding identity, we can rewrite Φ from (2.6) as

$$\begin{aligned} \Phi(\mathbf{x}) &= \int_V \frac{e^{-\|\mathbf{x} - \mathbf{x}'\|^2/2\sigma(\mathbf{x})^2}}{(2\pi\sigma(\mathbf{x}))^{3/2}} d\mathbf{x}' \\ &= - \int_V \Delta_{\mathbf{x}'} \left(\frac{\operatorname{Erf} \left(\frac{\|\mathbf{x} - \mathbf{x}'\|}{\sqrt{2}\sigma(\mathbf{x})} \right)}{4\pi\|\mathbf{x} - \mathbf{x}'\|} \right) d\mathbf{x}' \\ &= - \int_S \hat{\mathbf{N}}(\mathbf{x}') \cdot \nabla_{\mathbf{x}'} \left(\frac{\operatorname{Erf} \left(\frac{\|\mathbf{x} - \mathbf{x}'\|}{\sqrt{2}\sigma(\mathbf{x})} \right)}{4\pi\|\mathbf{x} - \mathbf{x}'\|} \right) da(\mathbf{x}') \\ &= \int_S \psi_\sigma(\mathbf{x}, \mathbf{x}') da(\mathbf{x}'), \end{aligned} \quad (4.3)$$

where

$$\psi_\sigma(\mathbf{x}, \mathbf{x}') = -\hat{\mathbf{N}}(\mathbf{x}') \cdot (\mathbf{x} - \mathbf{x}') \left(\frac{\operatorname{Erf} \left(\frac{\|\mathbf{x} - \mathbf{x}'\|}{\sqrt{2}\sigma(\mathbf{x})} \right)}{4\pi\|\mathbf{x} - \mathbf{x}'\|^3} - \frac{\sqrt{\frac{2}{\pi}} e^{-\|\mathbf{x} - \mathbf{x}'\|^2/2\sigma(\mathbf{x})^2}}{4\pi\sigma(\mathbf{x})\|\mathbf{x} - \mathbf{x}'\|^2} \right), \quad (4.4)$$

$$da(\mathbf{x}') = \|\mathbf{T}_u \times \mathbf{T}_v\| du dv,$$

and $\hat{\mathbf{N}}$ denotes the unit outward normal along the skeleton surface. The index j denoting individual triangles on the skeleton mesh has been suppressed in the above expressions. Note that we have made use of the divergence theorem to obtain the third line of (4.3).

In order to compute $\nabla\Phi$, we will also need to evaluate $\nabla\psi_\sigma$. From (4.3) and (4.4), we have

$$\begin{aligned} &\int_S \nabla_{\mathbf{x}} \psi_\sigma(\mathbf{x}, \mathbf{x}') dS(\mathbf{x}') \\ &= \int_S -\hat{\mathbf{N}}(\mathbf{x}') \left(\frac{\operatorname{Erf} \left(\frac{\|\mathbf{x} - \mathbf{x}'\|}{\sqrt{2}\sigma(\mathbf{x})} \right)}{4\pi\|\mathbf{x} - \mathbf{x}'\|^3} - \frac{\sqrt{\frac{2}{\pi}} e^{-\frac{\|\mathbf{x} - \mathbf{x}'\|^2}{2\sigma^2(\mathbf{x})}}}{4\pi\sigma(\mathbf{x})\|\mathbf{x} - \mathbf{x}'\|^2} \right) dS(\mathbf{x}') \\ &\quad + \int_S (\mathbf{x} - \mathbf{x}') F(\mathbf{x}, \mathbf{x}', \sigma) \left((\mathbf{x} - \mathbf{x}') \cdot \hat{\mathbf{N}}(\mathbf{x}') \right) dS(\mathbf{x}') \\ &\quad - \int_S \frac{e^{-\frac{\|\mathbf{x} - \mathbf{x}'\|^2}{2\sigma^2(\mathbf{x})}}}{\sigma^4(\mathbf{x})\pi^{3/2}2\sqrt{2}} \left((\mathbf{x} - \mathbf{x}') \cdot \hat{\mathbf{N}}(\mathbf{x}') \right) \nabla_{\mathbf{x}} \sigma(\mathbf{x}) dS(\mathbf{x}'), \end{aligned} \quad (4.5)$$

where

$$F(\mathbf{x}, \mathbf{x}', \sigma) = \frac{e^{-\frac{r^2}{2\sigma^2(\mathbf{x})}} \sqrt{2}(r^3 + 3r\sigma^2(\mathbf{x})) - 3\sqrt{\pi}\sigma^3(\mathbf{x}) \operatorname{Erf}\left(\frac{r}{\sqrt{2}\sigma(\mathbf{x})}\right)}{4\pi^{3/2}r^5\sigma(\mathbf{x})^3} \quad (4.6)$$

and $r = \|\mathbf{x} - \mathbf{x}'\|$.

4.2 Numerical evaluation of σ

Given the parameters λ and σ_0 which determine the shape of σ in (2.8), evaluation is straightforward. Having sorted the skeleton triangles into an octree data structure based on their centroids, the evaluation of the function σ is a purely local calculation due to the decay of the Gaussian kernels. Therefore, no fast algorithm is needed for its evaluation, merely maintaining an octree data structure is sufficient.

4.3 Numerical evaluation of Φ

We turn now to the numerical evaluation of the level set function $\Phi(\mathbf{x})$ and its gradient using (4.3) and (4.5). Since the kernels defining the integrands in (4.3) and (4.5) are smooth, we require only a high-order quadrature rule for smooth functions on triangles. For this purpose, we will make use of Vioreanu-Rokhlin rules [39], which also serve as interpolation nodes for polynomials on triangles.

Remark 2. *The Vioreanu-Rokhlin (VR) quadrature rules are Gaussian-like in that they integrate more functions than there are nodes in the quadrature. A perfect n -point Gaussian rule in two variables would exactly integrate $3n$ functions (as there are $3n$ parameters). In our case, let $n_q = (q+1)(q+2)/2$ denote the number of polynomials of total degree less than or equal to q in two variables. Using n_q nodes and weights, the Gaussian-like VR rules integrate exactly polynomials of u, v of total degree less than or equal to q' for some $q < q'$, and where $n_{q'} < 3n_q$. The relationship between q and q' is somewhat complicated, and we refer the reader to the original paper for details. For illustration, we note from [39], that with $q = 4$, there are 15 interpolation/quadrature nodes on the simplex, and that the VR quadrature rules integrate all polynomials of total degree less than or equal to $q' = 7$, of which there are 36 such functions.*

Once each skeleton triangle has been discretized using an n_q -point quadrature rule with nodes $\{u_k, v_k\}$ and weights $\{w_k\}$ on T_0 , we replace the surface integral representation for Φ in (4.3) with the discrete sum

$$\Phi(\mathbf{x}) \approx \sum_{j=1}^M \sum_{k=1}^{n_q} w_k \psi_\sigma(\mathbf{x} - \mathbf{T}^j(u_k, v_k)), \quad (4.7)$$

where \mathbf{T}^j is given in (3.1). This approximation is defined in all of \mathbb{R}^3 , and its level set $\Gamma_{1/2}$ (an approximation to the *true* level set) defines an analytic smooth surface.

Remark 3. *Note that the n_q nodes (quadrature nodes) for computing the integral in (4.7) are separate from the n_p nodes (discretization nodes) for obtaining a p th-order representation of the charts in 3.2. The quadrature nodes determine the continuous level set $\Gamma_{1/2}$ and the discretization determines the order of accuracy of the representation of $\Gamma_{1/2}$. In practice, it is often the case that q is chosen to be large so as to ensure the accurate evaluation of the integral, and p is of modest size.*

4.4 Fast multipole acceleration

Referring to (3.20), at the k th Newton iterate for computing the pseudonormal distance h_{ji} , we need to evaluate

$$\begin{aligned}\Phi(\mathbf{x}_{ji}^{(k)}) &= \sum_{\ell=1}^M \sum_{m=1}^{n_q} w_m \psi_\sigma(\mathbf{x}_{ji}^{(k)} - \mathbf{T}^\ell(u_m, v_m)), \\ \nabla\Phi(\mathbf{x}_{ji}^{(k)}) &= \sum_{\ell=1}^M \sum_{m=1}^{n_q} w_m \nabla\psi_\sigma(\mathbf{x}_{ji}^{(k)} - \mathbf{T}^\ell(u_m, v_m)),\end{aligned}\tag{4.8}$$

where

$$\mathbf{x}_{ji}^{(k)} = \mathbf{T}^j(u_i, v_i) + h_{ji}^{(k)} \mathbf{H}^j(u_i, v_i).\tag{4.9}$$

Thus, computing $\Phi(\mathbf{x}_{ji}^{(k)})$ and $\nabla\Phi(\mathbf{x}_{ji}^{(k)})$ boils down to computing N -body sums involving $n_q M$ sources and $n_p M$ targets for the kernels given by ψ_σ and $\nabla\psi_\sigma$. This computation can be accelerated using a variety of fast algorithms and evaluated in $\mathcal{O}((n_p + n_q)M)$ CPU time. In this section, we briefly describe one such approach, based on the fast multipole method for Laplace's equation. We refer the reader to [8, 21] for a thorough description of that method and to a sampling of the literature [4, 7, 16, 30, 37, 42] for related fast summation schemes. The exact FMM code used in our algorithm is based on the FMM3D library at github.com/flatironinstitute/fmm3d.

We first observe that once $r = \|\mathbf{x} - \mathbf{x}'\| \geq 8\sigma$,

$$\begin{aligned}|\text{Erf}(r/(\sqrt{2}\sigma)) - 1| &\leq 10^{-14}, \\ e^{-r^2/(2\sigma^2)} &\leq 1.5 \cdot 10^{-14}.\end{aligned}\tag{4.10}$$

Thus, at distances greater than 8σ , the kernel ψ_σ can be approximated to near double precision as

$$\psi_\sigma(\mathbf{x} - \mathbf{x}') \approx -\hat{\mathbf{N}}(\mathbf{x}') \cdot \nabla_{\mathbf{x}'} \left(\frac{1}{4\pi\|\mathbf{x} - \mathbf{x}'\|} \right).\tag{4.11}$$

The above expression is simply the kernel of the double layer potential for the Laplace operator, to which FMMs for Laplace potentials apply directly. More precisely, for any target point $\mathbf{x} \in \mathbb{R}^3$, we may write

$$\Phi(\mathbf{x}) \approx - \int_{S \setminus B_R(\mathbf{x})} \hat{\mathbf{N}}(\mathbf{x}') \cdot \nabla_{\mathbf{x}} \left(\frac{1}{4\pi\|\mathbf{x} - \mathbf{x}'\|} \right) da(\mathbf{x}') + \int_{S \cap B_R(\mathbf{x})} \psi_\sigma(\mathbf{x}, \mathbf{x}') da(\mathbf{x}'),\tag{4.12}$$

where $B_R(\mathbf{x})$ is a ball of radius R centered at \mathbf{x} with radius $R = R(\sigma(\mathbf{x}))$ chosen so that (4.11) is correct to the desired precision. The first term can be computed for all $\mathbf{x} \in \Gamma_{1/2}^{(k)}$ by the FMM in linear time. Here, $\Gamma_{1/2}^{(k)}$ denotes the k th approximation to the surface $\Gamma_{1/2}$ obtained during the Newton iteration described in Section 3.2. The second term in (4.12) is a purely local calculation, and can be carried out directly without the need for a fast algorithm. Assuming that $\sigma(\mathbf{x})$ is approximately of the same length scale as the nearest triangle and that the triangulation itself is multiscale but suitably graded, it is straightforward to show that the total cost for evaluating all such local interactions is $\mathcal{O}(M(n_p + n_q))$.

A naive implementation for evaluating $\psi_\sigma(\mathbf{x}, \mathbf{x}')$, however, is subject to catastrophic cancellation when \mathbf{x} is close to \mathbf{x}' ; since the expression for ψ_σ in (4.4) involves the difference

of two singular terms. Thus, for small values of $\|\mathbf{x} - \mathbf{x}'\|$, the kernel ψ_σ should be replaced by a suitable Taylor series approximation. Letting $u = \|\mathbf{x} - \mathbf{x}'\|/\sqrt{2}\sigma(\mathbf{x})$, a modest amount of algebra yields

$$\psi_\sigma(\mathbf{x}, \mathbf{x}') \approx \hat{\mathbf{N}}(\mathbf{x}') \cdot (\mathbf{x}' - \mathbf{x}) \left(\frac{\frac{2}{3} - \frac{2u^2}{5} + \frac{u^4}{7} - \frac{u^6}{27} + \frac{u^8}{132} + \dots}{4\sqrt{2\pi^3}\sigma(\mathbf{x})^3} \right), \quad (4.13)$$

with an error of about 10^{-13} so long as $u < 0.1$. For $u \geq 0.1$, the loss of accuracy from catastrophic cancellation in (4.4) is less than three digits of relative precision, and therefore at least thirteen digits of relative accuracy are obtained for any value of u using standard double precision arithmetic.

The gradient of Φ permits exactly the same decomposition. Contributions from the far field can be obtained directly from the FMM and the near field can be computed directly. The near field in (4.5) again involves the difference of singular terms but can be replaced by the Taylor series approximation

$$\begin{aligned} \frac{\partial\psi_\sigma(\mathbf{x}, \mathbf{x}')}{\partial x_i} \approx & -\hat{N}_i(\mathbf{x}') \left(\frac{\frac{2}{3} - \frac{2u^2}{5} + \frac{u^4}{7} - \frac{u^6}{27} + \frac{u^8}{132} + \dots}{4\sqrt{2\pi^3}\sigma(\mathbf{x})^3} \right) \\ & + \hat{\mathbf{N}}(\mathbf{x}') \cdot (\mathbf{x}' - \mathbf{x}) \left(\frac{e^{-u^2}}{2\sqrt{2\pi^3}\sigma(\mathbf{x})^4} \right) \frac{\partial\sigma(\mathbf{x})}{\partial x_i}, \end{aligned} \quad (4.14)$$

where $\hat{N}_i(\mathbf{x}')$ denotes the i th component of $\hat{\mathbf{N}}(\mathbf{x}')$.

4.5 Surface refinement

Since, as noted above, the level surface $\Gamma_{1/2}$ is defined by (4.7), it is a simple matter to refine the discretization so that the charts converge to $\Gamma_{1/2}$ with p th-order accuracy. One simply splits any skeleton triangle \mathbf{T}^j where refinement is desired into four subtriangles, adding the midpoints of each side as new vertices. In general, this procedure will break the earlier assumption of conformity of the skeleton mesh, but it is easy to check that the same refinement of the pseudonormal vector field remains continuous. One can then construct the pseudonormal vector fields on the subtriangles as above and solve the nonlinear equation (3.8) for each of the new quadrature nodes. Determining which sections of the geometry Γ^j need to be refined is up to the user, and standard *a posteriori* error estimates from adaptive interpolation or adaptive integration work well.

Remark 4. *The method described in this paper is based on the fundamental premise that the skeleton mesh is well enough resolved that the “nearby” C^∞ surface we construct can serve the purposes of the subsequent simulation. If $\Gamma_{1/2}$ is unsatisfactory, additional tools would be required that enable modification of the input triangulation. This is beyond the scope of the present work.*

5 Numerical examples

In this section we provide several numerical examples demonstrating the behavior and computational efficiency of our algorithm in converting flat skeleton triangulations into

higher order surfaces. In addition to computational scaling results, we also present results of computing a Gauss flux integral to estimate how *water-tight* the smooth surface is. To this end, let \mathbf{x}_0 denote some point in the interior of a region Ω with boundary Γ . It is easy to see that by straightforward application of the divergence theorem, and using the fact that the Green's function of the Laplace operator is $1/4\pi r$:

$$\begin{aligned}
1 &= \int_{\Omega} \delta(\mathbf{x}_0 - \mathbf{x}) dv(\mathbf{x}) \\
&= - \int_{\Omega} \Delta \frac{1}{4\pi\|\mathbf{x}_0 - \mathbf{x}\|} dv(\mathbf{x}) \\
&= - \int_{\Omega} \nabla \cdot \nabla \frac{1}{4\pi\|\mathbf{x}_0 - \mathbf{x}\|} dv(\mathbf{x}) \\
&= - \int_{\Gamma} \hat{\mathbf{N}}(\mathbf{x}) \cdot \nabla \frac{1}{4\pi\|\mathbf{x}_0 - \mathbf{x}\|} dv(\mathbf{x}).
\end{aligned} \tag{5.1}$$

The last expression is a measure of the flux through the surface Γ , and we therefore estimate the deviation of the output of our algorithm from a closed surface as ϵ_0 :

$$\epsilon_0 = 1 + \int_{\Gamma_{1/2}} \hat{\mathbf{N}}(\mathbf{x}) \cdot \nabla \frac{1}{4\pi\|\mathbf{x}_0 - \mathbf{x}\|} dv(\mathbf{x}). \tag{5.2}$$

In addition to reporting the value of ϵ_0 , tables containing results for the following numerical experiments also contain the data:

- M , the number of skeleton triangles,
- q , the order of Vioreanu-Rokhlin quadrature along S ,
- n_q , the number of quadrature nodes on each skeleton triangle,
- p , the order of the discretization of $\Gamma_{1/2}$,
- n_p , the number of nodes on each panel Γ^j ,
- k , number of Newton iterations,
- ϵ_N , max point-wise error in h after Newton iterations, as measured by

$$\epsilon_N = \max_{j,i} \left| h_{ji}^{(k)} - h_{ji}^{(k-1)} \right|, \tag{5.3}$$

- ϵ_0 , error in flux integral, described above,
- T_{FMM} , the time required for a single FMM call, i.e. time for one Newton iteration,

In each problem, the Newton iterations were run to a tolerance of 10^{-12} . In practice, the convergence of each Newton iteration for each discretization point along $\Gamma_{1/2}$ is independent, and therefore points (targets) that have already converged can be removed from the target list for subsequent FMM calls. A modest reduction in computational cost can be obtained by this optimization, but the overall scheme remains linear in cost and dominated by the initial Newton iterations.

Lastly, the algorithm was implemented in Fortran 77/95, and compiled with the Intel Fortran Compiler 2019. Examples were run on a workstation with 32 Intel Xeon Gold 6130 cores at 2.1GHz with 512GB of shared memory; modest multicore acceleration of the FMM was done using OpenMP directives. Plots of 3D images were created in Paraview [1].

5.1 Basic surface construction

In this example, we merely show the results of our algorithm when applied to a flat triangulation of a smooth surface, namely that of a cube with rounded edges and corners. The geometry was constructed in FreeCAD [32], exported as a `.step` file, and then imported and meshed in GiD v13.0.4 on Linux [26]. Two skeleton meshes are used in the example: one with 5736 flat triangles and a refined version with 21,852 flat triangles. The skeleton meshes and smoothed surfaces are shown in Figure 4. Data for this example is contained in Table 2. The original un-rounded cube has one vertex at $(0, 0, 0)$ and the opposite vertex at $(10, 10, 10)$. In order to test the Gauss flux integral, a point-source was placed at $(4.5, 4.5, 5)$.

Table 3 contains results from a refinement experiment. In this study, each of the skeleton triangles is refined into four sub-triangles, and the smoothing procedure is carried out again. While this refinement does not alter the skeleton surface, it does scale the width of the smoothing kernel σ , as well as result in a more resolved approximation of the smoothed surface (as shown by the convergence of ϵ_0). Near machine precision water-tightness is relatively easy to achieve.

5.2 Recovery of a sphere

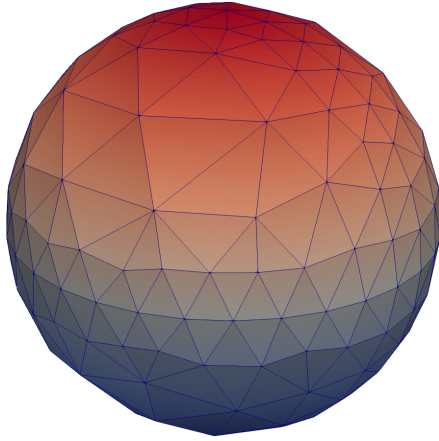
In this example, we obtain a smooth surface from a rough flat triangulations of a sphere. Figure 3 illustrates an example skeleton mesh and the smooth surface obtained using the algorithm of this work. As an additional measure, we also report the average of the norm of the discretization points (i.e. distance from the origin) on the smooth surface, as well as the standard deviation:

$$\langle \mathbf{x} \rangle = \frac{1}{Mn_p} \sum_{i=1}^M \sum_{j=1}^{n_p} \|\mathbf{x}_{ij}\|, \quad \text{std}(\mathbf{x}) = \sqrt{\frac{1}{Mn_p} \sum_{i=1}^M \sum_{j=1}^{n_p} (\|\mathbf{x}_{ij}\| - \langle \mathbf{x} \rangle)^2} \quad (5.4)$$

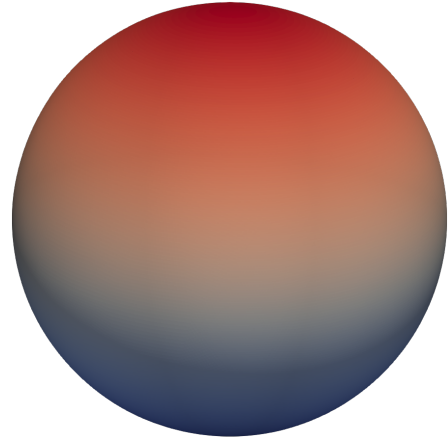
Table 1 contains results. In order to check the Gauss integral, a point source was placed at $(0.1, 0, 0)$. The triangulation was obtained directly from GiD [26], and little effort was made to ensure that it was regular. Clearly there is a modest amount of adaptive refinement near the edges of the CAD surfaces, but such features are not visible in the smoothed geometry. Lastly, note that Table 1 contains the dual information as Table 2: p is varied for fixed q , instead of vice versa. In summary, the smooth surface is a smooth sphere-like object that deviates from true sphere by roughly 0.01, albeit with a radius not equal to one. This is quite good, as the original skeleton mesh was not particularly fine.

Table 1: Results for smoothing a triangulation of a sphere.

M	q	n_q	Mn_q	p	n_p	Mn_p	k	ϵ_N	ϵ_0	T_{FMM}	$\langle \mathbf{x} \rangle$	$\text{std}(\mathbf{x})$
416	4	15	6240	4	15	6240	4	4.2 E-13	9.6 E-08	1.1 E+00	0.96473	1.4 E-02
416	4	15	6240	8	45	18,720	4	9.6 E-13	6.2 E-13	3.1 E+00	0.96375	1.4 E-02
416	4	15	6240	12	91	37,856	4	1.0 E-12	3.0 E-15	6.4 E+00	0.96375	1.4 E-02
416	8	45	18,720	4	15	6240	4	9.8 E-13	9.6 E-07	3.5 E+00	0.96373	1.4 E-02
416	8	45	18,720	8	45	18,720	4	6.9 E-13	3.9 E-13	9.1 E+00	0.96375	1.4 E-02
416	8	45	18,720	12	91	37,856	4	1.0 E-12	2.2 E-15	1.9 E+01	0.96375	1.4 E-02



(a) The skeleton mesh.



(b) The smoothed surface.

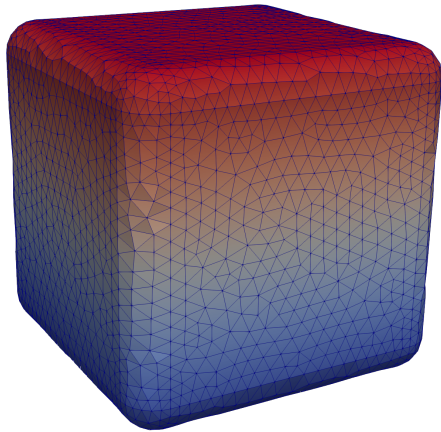
Figure 3: Skeleton and smooth surfaces for a sphere. The skeleton mesh contains 416 triangles. The skeleton surface was discretized using 4th-order quadratures, and the smoothed surface is piecewise 4th-order smooth.

Table 2: Results for smoothing a triangulation of a rounded cube.

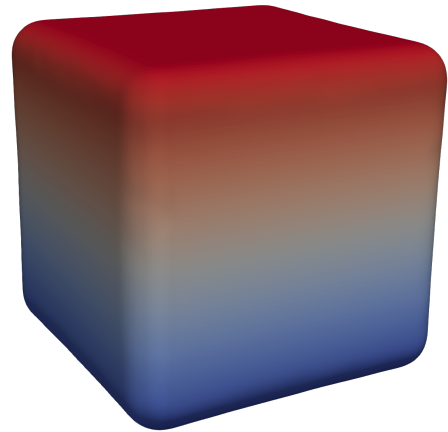
M	q	n_q	Mn_q	p	n_p	Mn_p	k	ϵ_N	ϵ_0	T_{FMM}
5736	4	15	86,040	4	15	86,040	4	1.0 E-12	1.1 E-07	5.9 E+00
5736	8	45	258,120	4	15	86,040	4	1.0 E-12	1.1 E-07	1.1 E+01
5736	12	91	521,976	4	15	86,040	4	1.0 E-12	1.1 E-07	1.9 E+01
5736	4	15	86,040	8	45	258,120	4	1.0 E-12	4.7 E-13	1.5 E+01
5736	8	45	258,120	8	45	258,120	4	1.1 E-12	4.8 E-13	2.9 E+01

Table 3: Convergence under refinement for smoothing a triangulation of a rounded cube.

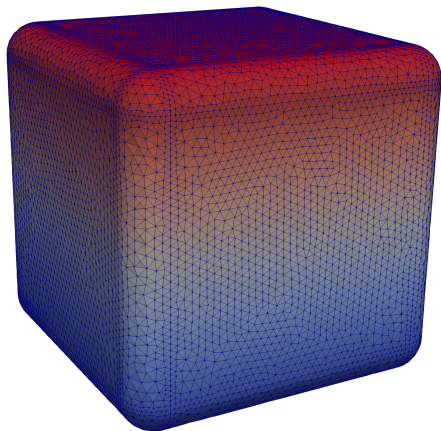
M	q	n_q	Mn_q	p	n_p	Mn_p	k	ϵ_N	ϵ_0	T_{FMM}
5736	4	15	86,040	4	15	86,040	4	1.0 E-12	1.1 E-07	5.9 E+00
22,944	4	15	344,160	4	15	344,160	3	1.0 E-12	1.9 E-10	1.9 E+01
91,776	4	15	1,376,640	4	15	1,376,640	2	1.0 E-12	4.6 E-13	7.2 E+01



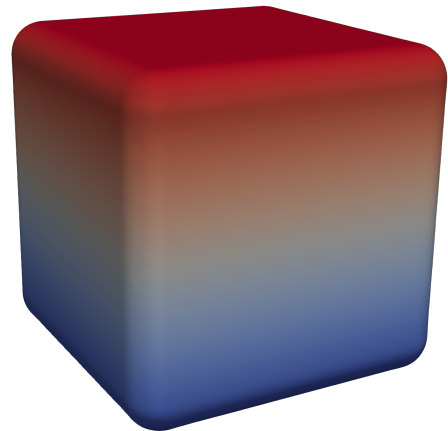
(a) Skeleton mesh.



(b) Smoothed surface from 4a.



(c) Skeleton mesh.



(d) Smoothed surface from 4c.

Figure 4: Skeleton and smooth surfaces for a rounded cube. The skeleton mesh in 4a contains 5736 flat triangles, and the resulting smoothed surface in 4b is piecewise 4th-order. The skeleton mesh in 4c contains 21,852 flat triangles, and the resulting smoothed surface in 4c is piecewise 4th-order. In each case, the integral defining the level set was discretized using 4th-order Vioreanu-Rokhlin quadratures.

5.3 Quadratic skeletons

A torus is one of the smooth primitives in the software GiD [26], and therefore a straightforward test. In this example, we show the remarkable increase in quality of the smooth surface when the skeleton mesh consists of quadratic patches (i.e. 2nd-order curvilinear triangles) instead of flat triangles. In order to clearly demonstrate the benefit, we have set $\lambda = 10$ in (2.8) (the scaling parameter for the width of the convolution kernel). This narrows the width of the convolving kernel, which allows for preservation of more fine-scale features of the actual skeleton mesh. We only present images as qualitative results in this case, as the various convergence results are similar to the previous two examples. It is worth pointing out that quadratic triangles can easily be shown to form an exact water-tight surface, and therefore the construction of our pseudonormal vector field is analogous to the case in which the skeleton mesh consists of flat triangles.

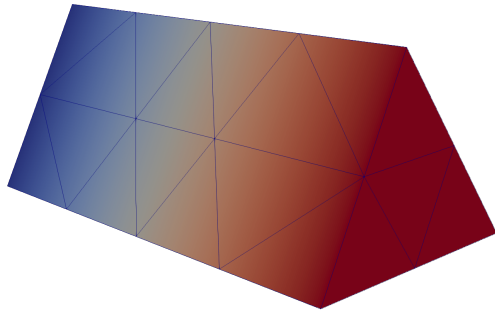
5.4 Large-scale structures

In this section we demonstrate the performance of our algorithm on a relatively large-scale structure with highly multiscale features. Figure 7 contains images of the skeleton mesh and resulting smoothed surface for a mock-up of an A380 passenger aircraft with small antennas mounted on the top. The geometry was designed and meshed in GiD v13.0.4. The skeleton mesh consists of 31,336 quadratic curvilinear triangles. Each skeleton patch was discretized using a 4th order Vioreanu-Rokhlin quadrature, we set $\lambda = 10$, and the smooth surface was computed to 4th order as well. Despite the existence of edges on the multiscale antennas, as seen in the figures, the algorithm does a qualitatively good job of obtaining a nearby smooth surface without any noticeable ringing artifacts. Convergence in the divergence test is of high-order, and the FMM scales linearly (as expected). This data is presented in Table 4.

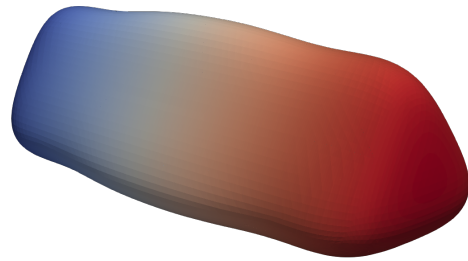
5.5 Modes of failure

There is one main regime in which our algorithm does not produce qualitatively acceptable results: when the skeleton mesh is too coarse. On the one hand, since our algorithm is attempting to recover a smooth surface nearby to the skeleton mesh, if the skeleton mesh is very coarse the argument could be made that it is not a good approximation of an underlying smooth surface. On the other hand, there are many geometries in which a coarse mesh is an exact description of the geometry, for example 12 flat triangles exactly describe the surface of a cube.

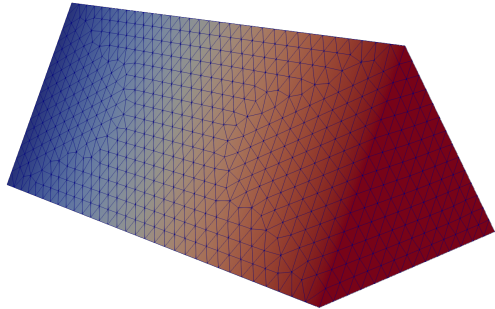
When the mesh is globally coarse, it can be shown that the level set function Φ develops oscillations. This is most easily seen in 2D by examining the level sets (curves) of the convolution of a Gaussian with the indicator function of the unit square. We refer to this behavior as *geometric ringing*, inspired by similar behavior that arises in signal processing applications (i.e. Fourier aliasing and filtering). A simple three-dimensional example is shown in Figure 5. Notice also, in Figure 5b, that the volume/dimensions of the object shrink noticeably when a very coarse mesh is used as a skeleton surface. The mesh was sufficiently coarse in this example that the algorithm failed to find a level set during the Newton iterations with $\lambda = 2.5$. Setting $\lambda = 10$ resulted in convergence to a level set, and preserved more local feature of the geometry.



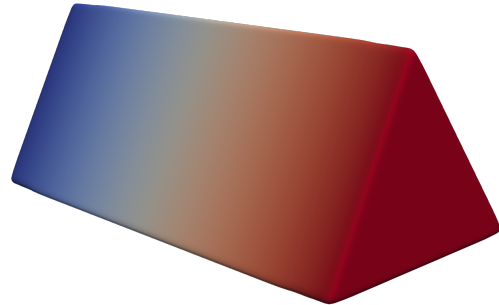
(a) A very coarse skeleton mesh with 50 elements.



(b) A naive smoothing of coarse mesh with $\lambda = 5$.

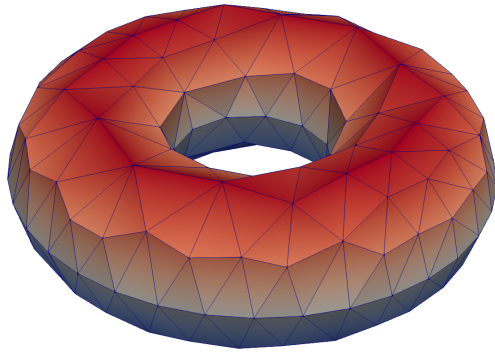


(c) A refined skeleton mesh with 3368 elements.

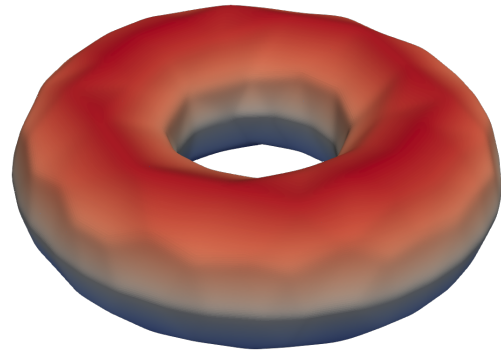


(d) A smoothing of the refined mesh with $\lambda = 5$.

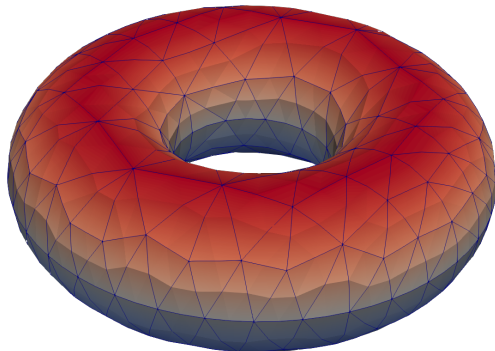
Figure 5: The main mode of failure of the algorithm of this work, so-called *geometric ringing*. Qualitatively, the skeleton mesh is not a good approximation of an underlying smooth surface in the top figures. With some refinement, as in the bottom figures, the results are qualitatively more pleasing.



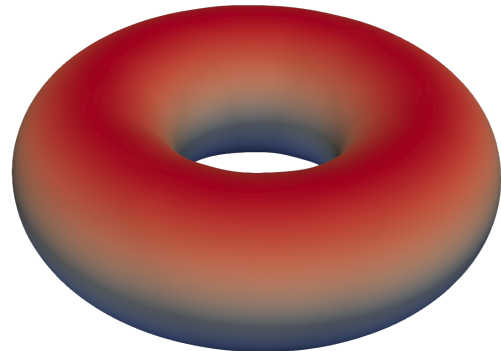
(a) A flat skeleton.



(b) $\Phi_{1/2}$ from flat skeleton.



(c) A quadratic skeleton.



(d) $\Phi_{1/2}$ from quadratic skeleton.

Figure 6: A qualitative comparison of the improvement when using quadratic skeleton meshes instead of flat ones. In each case, the skeleton surface was discretized using 12th-order quadratures, and the smoothed surface is piecewise smooth to 12th-order. In both examples, the Gauss integral was accurate to approximately 9 digits.

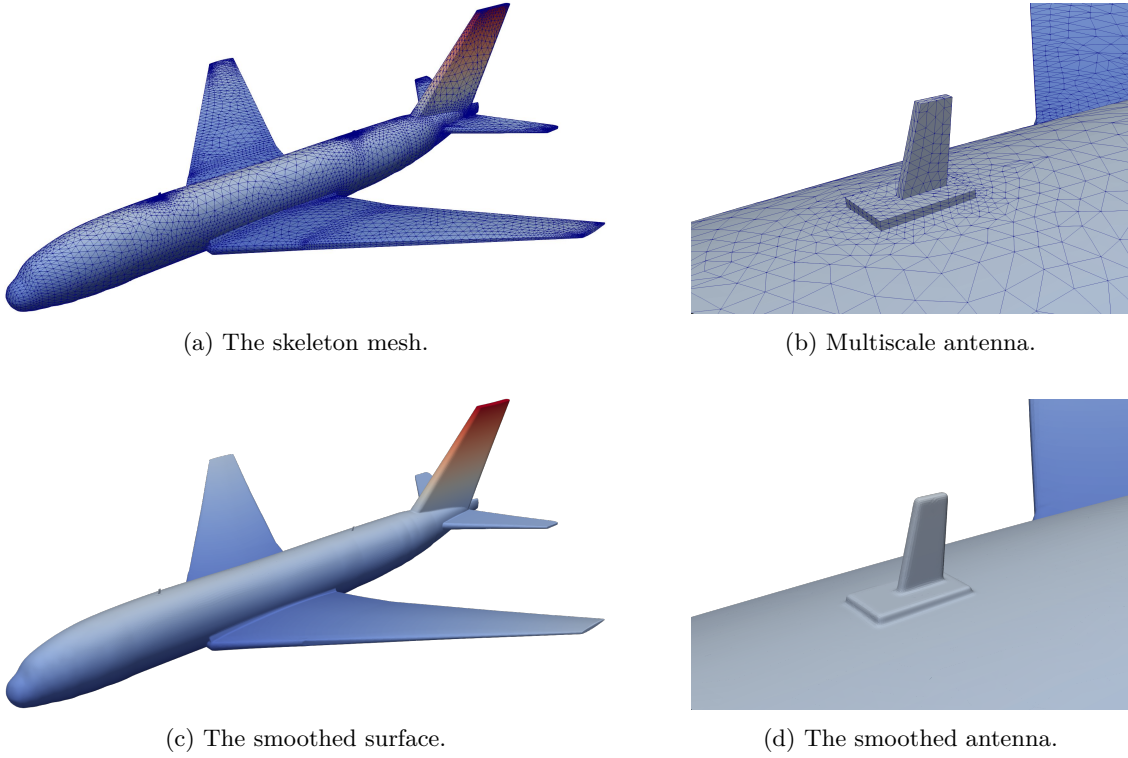


Figure 7: Quadratic skeleton mesh and smooth surfaces for a model passenger airplane. The skeleton mesh contains 31,336 quadratic triangles, and the smoothed surface is piecewise 4th-order smooth.

Table 4: Convergence under refinement for smoothing a quadratic triangulation of a passenger airplane.

M	q	n_q	Mn_q	p	n_p	Mn_p	k	ϵ_N	ϵ_0	T_{FMM}
31,336	4	15	470,040	4	15	470,040	4	1.0 E-12	1.5 E-06	1.8 E+01
125,344	4	15	1,880,160	4	15	1,880,160	4	1.0 E-12	2.1 E-08	6.3 E+01
501,376	4	15	7,520,640	4	15	7,520,640	4	1.0 E-12	3.6 E-10	2.5 E+02

6 Conclusions

In this work, we have presented a multiscale algorithm which is able to construct arbitrarily high-order piecewise smooth surfaces using only a skeleton mesh. In practice, this usually consists of a water-tight flat triangulation as input. The algorithm uses a target-dependent smoothing kernel, which is designed to be commensurate with the local mesh size. The resulting smooth surface is constructed as an atlas of charts from the skeleton triangles to a well-defined level set. The scheme is accelerated via reformulation as a boundary integral and the use of a fast multipole method; several numerical experiments illustrate the performance of the approach.

It is worth reminding the reader of the principal mode of failure of the algorithm: significant geometric artifacts will be generated when the initial skeleton mesh does not accurately represent an underlying smooth surface. That is to say, when the skeleton triangles are not scaled to be commensurate with rapid changes in geometric features (such as the normal direction), we observe what we referred to as *geometric ringing*, in which the smooth surface develops oscillations. This behavior can be ameliorated by refining the skeleton mesh to the desired length scale of smoothing.

Going forward, there are two important scenarios that we have not addressed, but that are the focus of current work: (1) extending the algorithm to skeleton meshes that are *not* water-tight, and noisy (e.g. those obtained from a 3D scanning procedure), and (2) permitting the inclusion of singular features (such as corners and edges) which are to be left intact as part of the smoothing process. The algorithm, as it is currently implemented, smooths away geometric singularities at the length scale of the triangles impinging on the relevant feature. We are also investigating the use of our surface smoothing framework for problems involving surface motion or surface remeshing.

Acknowledgments

We gratefully acknowledge the support of the NVIDIA Corporation with the donation of a Quadro P6000, used for some of the visualizations presented in this research.

References

- [1] J. Ahrens, B. Geveci, and C. Law. Paraview: An end-user tool for large data visualization. *The visualization handbook*, 717, 2005.
- [2] J. F. Blinn. A Generalization of Algebraic Surface Drawing. *ACM Trans. Graphics*, 1:235–256, 1982.
- [3] J. Bloomenthal and K. Shoemake. Convolution surfaces. *SIGGRAPH Comput. Graph.*, 25(4):251–256, July 1991.
- [4] S. Börm, L. Grasedyck, and W. Hackbusch. Introduction to hierarchical matrices with applications. *Engineering Analysis with Boundary Elements*, 27(5):405–422, 2003.
- [5] J. Bremer, A. Gillman, and P.-G. Martinsson. A high-order accelerated direct solver for integral equations on curved surfaces. *BIT Num. Math.*, 55:367–397, 2015.

- [6] O. P. Bruno and L. A. Kunyansky. A fast, high-order algorithm for the solution of surface scattering problems: Basic implementation, tests, and applications. *J. Comput. Phys.*, 169(1):80–110, 2001.
- [7] H. Cheng, W. Y. Crutchfield, Z. Gimbutas, L. Greengard, J. F. Ethridge, J. Huang, V. Rokhlin, N. Yarvin, and J. Zhao. A wideband fast multipole method for the Helmholtz equation in three dimensions. *J. Comput. Phys.*, 216:300–325, 2006.
- [8] H. Cheng, L. Greengard, and V. Rokhlin. A fast adaptive multipole algorithm in three dimensions. *J. Comput. Phys.*, 155(2):468–498, 1999.
- [9] R. Coifman, V. Rokhlin, and S. Wandzura. The fast multipole method for the wave equation: A pedestrian prescription. *IEEE Antennas Propag. Mag.*, 35(3):7–12, 1993.
- [10] J. A. Cottrell, T. J. R. Hughes, and Y. Bazilevs. *Isogeometric Analysis: Toward Integration of CAD and FEA*. Wiley, West Sussex, UK, 2009.
- [11] C. Dapogny, C. Dobrzynski, and P. Frey. Three-dimensional adaptive domain remeshing, implicit domain meshing, and applications to free and moving boundary problems. *J. Comput. Phys.*, 262:358–378, 2014.
- [12] E. Darve and P. Havé. A fast multipole method for Maxwell equations stable at all frequencies. *Philosophical Transactions of the Royal Society of London A: Mathematical, Physical and Engineering Sciences*, 362(1816):603–628, 2004.
- [13] T. DeRose, M. Kass, and T. Truong. Subdivision surfaces in character animation. In *Proceedings of the 25th annual conference on Computer graphics and interactive techniques*, pages 85–94. ACM, 1998.
- [14] C. L. Epstein and M. O’Neil. Smoothed corners and scattered waves. *SIAM J. Sci. Comput.*, 38:A2665–A2698, 2016.
- [15] S. Fleishman, D. Cohen-Or, and C. T. Silva. Robust moving least-squares fitting with sharp features. *ACM Trans. Graph.*, 24(3):544–552, July 2005.
- [16] W. Fong and E. Darve. The black-box fast multipole method. *J. Comput. Phys.*, 228(23):8712–8725, 2009.
- [17] K. O. Friedrichs. On the differentiability of the solutions of linear elliptic differential equations. *Commun. Pure Appl. Math.*, 6:299–325, 1953.
- [18] C. Geuzaine and J.-F. Remacle. Gmsh: A 3-D finite element mesh generator with built-in pre- and post-processing facilities. *Int. J. Num. Methods Engrg.*, 79:1309–1331, 2009.
- [19] A. Greenbaum, L. Greengard, and G. B. McFadden. Laplace’s equation and the Dirichlet-Neumann map in multiply connected domains. *J. Comput. Phys.*, 105(2):267–278, 1993.
- [20] L. Greengard and V. Rokhlin. A Fast Algorithm for Particle Simulations. *J. Comput. Phys.*, 73:325–348, 1987.

- [21] L. Greengard and V. Rokhlin. A new version of the Fast Multipole Method for the Laplace equation in three dimensions. *Acta Numerica*, 6:229–269, 1997.
- [22] S. Hao, A. H. Barnett, P.-G. Martinsson, and P. Young. High-order accurate Nyström discretization of integral equations with weakly singular kernels on smooth curves in the plane. *Adv. Comput. Math.*, 40:245–272, 2014.
- [23] J. Helsing and R. Ojala. Corner singularities for elliptic problems: Integral equations, graded meshes, quadrature, and compressed inverse preconditioning. *J. Comput. Phys.*, 227(20):8820–8840, 2008.
- [24] Y. Hu, Q. Zhou, X. Gao, A. Jacobson, D. Zorin, and D. Panozzo. Tetrahedral meshing in the wild. *ACM Trans. Graph.*, 37:Article 60, 2018.
- [25] T. J. Hughes, J. A. Cottrell, and Y. Bazilevs. Isogeometric analysis: CAD, finite elements, NURBS, exact geometry and mesh refinement. *Computer methods in applied mechanics and engineering*, 194(39-41):4135–4195, 2005.
- [26] International Center for Numerical Methods in Engineering (CIMNE) . GiD: The personal pre and post processor. www.gidhome.com, 2017.
- [27] T. Koornwinder. Two-variable analogues of the classical orthogonal polynomials. In *Theory and application of special functions (Proc. Advanced Sem., Math. Res. Center, Univ. Wisconsin, Madison, Wis., 1975)*, pages 435–495. Academic Press New York, 1975.
- [28] P.-G. Martinsson and V. Rokhlin. A fast direct solver for boundary integral equations in two dimensions. *J. Comput. Phys.*, 205:1–23, 2005.
- [29] M. O’Neil. Second-kind integral equations for the Laplace-Beltrami problem on surfaces in three dimensions. *Adv. Comput. Math.*, 44(5):1385–1409, 2018.
- [30] J. Phillips and J. White. A precorrected-FFT method for electrostatic analysis of complicated 3-D structures. *IEEE Trans. Computer-Aided Design*, 16(10):1059–1072, 1997.
- [31] M. Rachh, A. Klöckner, and M. O’Neil. Fast algorithms for Quadrature by Expansion I: Globally valid expansions. *J. Comput. Phys.*, 345:706–731, 2017.
- [32] J. Riegel, W. Mayer, and Y. van Havre. FreeCAD, v. 0.18.1, 2019. <http://www.freecadweb.org/>.
- [33] A. Sherstyuk. Interactive shape design with convolution surfaces. In *Proceedings Shape Modeling International ’99. International Conference on Shape Modeling and Applications*, pages 56–65, March 1999.
- [34] A. Sherstyuk. Kernel functions in convolution surfaces: a comparative analysis. *Visual Comput.*, 15:171–182, 1999.
- [35] M. Siegel and A.-K. Tornberg. A local target specific quadrature by expansion method for evaluation of layer potentials in 3D. *J. Comput. Phys.*, 364:365–392, 2018.

- [36] R. N. Simpson, M. A. Scott, M. Taus, D. C. Thomas, and H. Lian. Acoustic isogeometric boundary element analysis. *Computer Methods in Applied Mechanics and Engineering*, 269:265–290, 2014.
- [37] J. Song, C.-C. Lu, and W. C. Chew. Multilevel fast multipole algorithm for electromagnetic scattering by large complex objects. *IEEE Trans. Antennas Propag.*, 45(10):1488–1493, 1997.
- [38] J. Strain. The fast Gauss transform with variable scales. *SIAM Journal on Scientific and Statistical Computing*, 12(5):1131–1139, 1991.
- [39] B. Vioreanu and V. Rokhlin. Spectra of Multiplication Operators as a Numerical Tool. *SIAM J. Sci. Comput.*, 36:A267–A288, 2014.
- [40] M. Wala and A. Klöckner. A Fast Algorithm for Quadrature by Expansion in Three Dimensions. *arXiv [math.NA]*, 1805.06106, 2018.
- [41] J. Wang and L. Greengard. An adaptive fast Gauss transform in two dimensions. *SIAM J. Sci. Comput.*, 40:A1274–A1300, 2018.
- [42] L. Ying, G. Biros, and D. Zorin. A high-order 3D boundary integral equation solver for elliptic PDEs in smooth domains. *J. Comput. Phys.*, 219(1):247–275, 2006.
- [43] L. Ying and D. Zorin. A simple manifold-based construction of surfaces of arbitrary smoothness. *ACM Trans. Graphics*, 23(3):271–275, 2004.
- [44] D. Zorin, P. Schröder, and W. Sweldens. Interpolating subdivision for meshes with arbitrary topology. In *Proceedings of the 23rd annual conference on Computer graphics and interactive techniques*, pages 189–192. ACM, 1996.